



Full length article

Multi-scale characterization of the spatio-temporal interplay between elemental composition, mineral deposition and remodelling in bone fracture healing

Hector Dejea^{a,b}, Deepak Bushan Raina^c, Isabella Silva Barreto^a, Kunal Sharma^a, Yang Liu^c, Dario Ferreira Sanchez^d, Ulf Johansson^b, Hanna Isaksson^{a,*}

^a Department of Biomedical Engineering, Lund University, Box 118, 221 00 Lund, Sweden

^b MAX IV Laboratory, Lund University, Box 118, 221 00 Lund, Sweden

^c Orthopedics, Department of Clinical Sciences, Lund University, Box 118, 221 00 Lund, Sweden

^d Photon Science Division, Swiss Light Source, 5232 Villigen-PSI, Switzerland

ARTICLE INFO

Article history:

Received 31 March 2023

Revised 16 June 2023

Accepted 22 June 2023

Available online 25 June 2023

Keywords:

Bone mineralization

Endochondral ossification

Fracture healing

Multi-scale

Multi-modal

ABSTRACT

Bone mineralization involves a complex orchestration of physico-chemical responses from the organism. Despite extensive studies, the detailed mechanisms of mineralization remain to be elucidated. This study aims to characterize bone mineralization using an *in-vivo* long bone fracture healing model in the rat. The spatio-temporal distribution of relevant elements was correlated to the deposition and maturation of hydroxyapatite and the presence of matrix remodeling compounds (MMP-13). Multi-scale measurements indicated that (i) zinc is required for both the initial mineral deposition and resorption processes during mature mineral remodeling; (ii) Zinc and MMP-13 show similar spatio-temporal trends during early mineralization; (iii) Iron acts locally and in coordination with zinc during mineralization, thus indicating novel evidence of the time-events and inter-play between the elements. These findings improve the understanding of bone mineralization by explaining the link between the different constituents of this process throughout the healing time.

Statement of significance

Bone mineralization involves a complex orchestration of physico-chemical responses from the organism, the detailed mechanisms of which remain to be elucidated. This study presents a highly novel multi-scale multi-modal investigation of bone mineralization using bone fracture healing as a model system. We present original characterization of tissue mineralization, where we relate the spatio-temporal distribution of important trace elements to a key matrix remodeling compound (MMP-13), the initial deposition and maturation of hydroxyapatite and further remodeling processes. This is the first time that mineralization has been probed down to the nanometric level, and where key mineralization components have been investigated to achieve a comprehensive and mechanistic understanding of the underlying mineralization processes during bone healing.

© 2023 The Authors. Published by Elsevier Ltd on behalf of Acta Materialia Inc.

This is an open access article under the CC BY license (<http://creativecommons.org/licenses/by/4.0/>)

* Corresponding author at: Department of Biomedical Engineering, Lund University, Box 118, 221 00 Lund, Sweden.

E-mail addresses: hector.dejea@bme.lth.se (H. Dejea), deepak.raina@med.lu.se (D.B. Raina), isabella.silva_barreto@bme.lth.se (I. Silva Barreto), kunal.sharma@bme.lth.se (K. Sharma), liu.yang@med.lu.se (Y. Liu), dario.ferreira@psi.ch (D. Ferreira Sanchez), ulf.johansson@maxiv.lu.se (U. Johansson), hanna.isaksson@bme.lth.se (H. Isaksson).

1. Introduction

Bone mineralization generally occurs through primary (intra-membranous ossification) or secondary (endochondral ossification) bone formation. In the latter, an initial cartilaginous matrix serves as a template for mineralization [1,2]. Despite extensive studies to understand bone mineralization at the cellular and molecular levels, the biophysical and biochemical mechanisms by which the cartilaginous callus is mineralized remain unclear. In particular, the transition from when the first amorphous calcium

phosphate (CaP) crystals are laid out and their consequent maturation into crystalline hydroxyapatite (HA) and the role of different trace elements involved in the mineralization process is not well defined in an *in-vivo* setting. Many theories have been proposed to describe these mechanisms, but most experiments have been based on *in-vitro* studies conducted under well-controlled experimental conditions [3–7], often without considering the multitude of biological processes that occur during bone mineralization. However, studies on mineral deposition and the underlying mechanisms from an elemental composition perspective in *in-vivo* animal models are sparse [6–9].

Long bone fracture healing can be used as a model of mineralization as it involves/re-capitulates both ossification pathways. Fracture healing is a regenerative process involving a complex series of cellular and molecular responses that resemble the events occurring during embryonic bone development [10]. The regeneration is complete so that, in most cases, the damaged bone fully recovers its previous biological, structural, and biomechanical properties without the formation of scar tissue [11,12]. The intricate cascade of events occurring during regeneration in long bones begins with an acute inflammatory response followed by the recruitment of mesenchymal stem cells, which start differentiating into phenotype specific cells able to form a range of skeletal tissues and vasculature. Firstly, osteoblasts lay down a non-mineralized osteoid matrix which eventually mineralizes. Fractures that are not mechanically stable or where the distance between the broken bone ends is large, primarily heal via the endochondral ossification route. In that case, an initial cartilaginous matrix is formed, which later undergoes neo-vascularization, degradation, and mineralization. This secondary mineralization leads to the formation of the “final” hard callus that bridges the fracture. Remodeling of the hard callus is a continual physiological process until the bone is restored with its previous biomechanical properties [11–13].

Fracture healing via the endochondral ossification route relies predominantly on the remodeling of the cartilage matrix during the cartilage to bone transition. This transition is an intricate biochemically regulated process in which matrix metalloproteinase-13 (MMP-13), a member of the Zn-dependent endopeptidase family, has been shown to play a pivotal role [14]. MMP-13 deficient embryos have been shown to possess large hypertrophic zones in the growth plate and delayed formation of the primary ossification centers, both of which are indicative of reduced cartilage resorption [15]. Interestingly, similar to embryonic skeletal development, MMP-13 null mice also have a significant impairment in fracture healing where the healing is delayed due to retarded cartilage clearance from the fracture site [14].

Mineralization is regulated not only by the levels of Ca, but also other trace elements such as Zn, Fe, Pb, Cu or Sr, among others [16–18]. While being present in very small quantities, maintaining the appropriate concentration and spatial distribution of trace elements is key for healthy bone tissue. This becomes especially important in metabolically active processes such as fracture healing. However, the roles of these elements and how they correlate with other structural properties still needs to be elucidated.

To approach a more comprehensive understanding of mineralization and fracture healing, especially given the hierarchical nature of bone and the variety of biological and molecular processes involved, multi-modal and multi-scale analysis approaches are paramount. At the macro-/mesoscopic scales, micro-computed tomography (microCT) is state of the art to assess the evolution of tissue mineralization [9,19]. To probe events occurring at the (sub)cellular level, high resolution structural and elemental characterization techniques are required. For this purpose, synchrotron light sources have been proven to provide valuable methods for

biomedical research at different length scales, down to the micrometer and nanometer level [20,21]. Scattering techniques such as small- and wide-angle x-ray scattering (SAXS, WAXS) have been previously exploited to investigate HA crystal orientation, thickness (T-parameter), length (L-parameter) and width (W-parameter) in diverse animal models of mineralization [22–30]. Moreover, in terms of elemental analysis, x-ray fluorescence (XRF) has been widely used to explore the presence and role of trace elements in the bone formation process [16,17,31]. Finally, gold-standard biological tissue characterization techniques such as histology and immunohistochemistry allow to study the spatial distribution of relevant tissues and key matrix remodeling compounds directly participating in mineralization, such as MMP-13 [32].

In this study, we aim to investigate bone mineralization in an *in-vivo* long bone fracture healing model [9]. This is achieved in a multi-modal and multi-scale approach by progressively following the mineralization front (at the bone-cartilage interface) in bone samples obtained at different time-points representative of the different healing stages [12]. In doing so, we correlate the distribution and presence of different elements with initial mineral deposition, the development to mature HA nanocrystals and their spatial relation to matrix remodeling compounds such as MMP-13. Therefore, we aim to correlate the spatial distribution of matrix remodeling compounds with the physico-chemical composition of the extracellular matrix with a novel approach from the micro- and down to the nano-scale.

2. Materials and methods

The overall approach is illustrated in Fig. 1, while a description of the number of samples studied with each technique can be found in Table 1.

2.1. Animal model

A total of 19 Sprague-Dawley rats (male, average weight: 323 ± 53 g) were used in this study. Rats were caged in pairs with a temperature of 21 °C, a 12 h light/dark cycle and provided with food and water *ad libitum*. During surgery, the animals were anesthetized using isoflurane (induction: 3%, maintenance: 2%) with a mixture of oxygen at a flow rate of 0.4 L/min. A well established *in-vivo* open fracture model was used to create an osteotomy in the mid diaphysis of the femur [9,33]. The fracture was created using a gigly wire to minimize heat induced injury to the bone ends and stabilized with a Kirshner-wire (k-wire) with a diameter of 1.1 mm. This provides partial compressional stability but not rotational stability to the bone, thus causing the formation of a large callus and mainly inducing bone formation via the endochondral pathway. Post-surgical pain management was performed using morphine (25 µg/kg), administered subcutaneously, twice daily for a total duration of 72 h. Rats were euthanized using CO₂ asphyxiation at days 7 ($n = 4$), 10 ($n = 4$), 14 ($n = 4$), 21 ($n = 4$) and 28 ($n = 3$) to progressively investigate fracture healing and the mineralization front with a range of imaging techniques.

The animal experiments adhered to the institutional guidelines for the care and treatment of laboratory animals. The study was approved by the Regional Ethics Committee for animal experiments in Malmö-Lund, Sweden (Jordbruksverket, permit number: 18-08106/2018), and was performed in compliance with the ARRIVE Guidelines.

2.2. Micro-computed tomography

Healing femurs were scanned in two batches ($n = 9$, for synchrotron experiments, and $n = 10$, for histological procedures) at

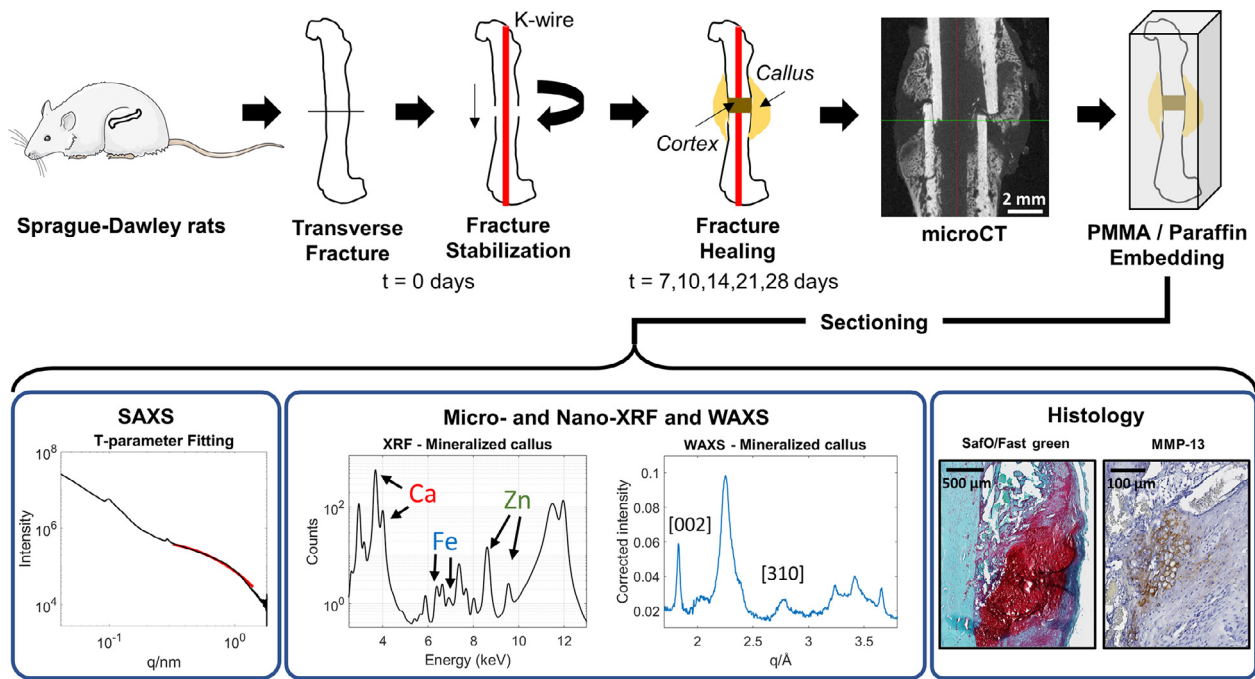


Fig. 1. A schematic of the study plan summarizing the methodology and different techniques used in the characterization of different stages in endochondral fracture healing.

Table 1

Number of samples analyzed with each of the techniques. All femurs ($n = 19$) were scanned in microCT. Batch 1 ($n = 9$) was prepared for synchrotron experiments. Batch 2 was prepared for histological measurements. HAp refers to HA microparticles.

	All, $n = 19$ femurs		Batch 1, $n = 9$ femurs		Batch 2, $n = 10$ femurs
	microCT	SAXS	Microscale XRF & WAXS	Nanoscale XRF & WAXS	Histology Safo/Fast green & MMP-13
	# femurs	# sections	# sections	# sections	# femurs
Day 7	$n = 4$	-	$n = 1^*$	$n = 1^*$	$n = 2$
Day 10	$n = 4$	$n = 1$	$n = 1^*$	$n = 1^*$	$n = 2$
Day 14	$n = 4$	$n = 1$	$n = 1$	$n = 1$	$n = 2$
Day 21	$n = 4$	$n = 1$	$n = 1^*$	$n = 1^*$	$n = 2$
Day 28	$n = 3$	-	$n = 1$	$n = 1$	$n = 2$
Cortex	$n = 19^{**}$	-	$n = 1$	$n = 1$	$n = 10^{**}$
HAp	-	-	-	$n = 1$	-

* Indicates same slice for both microscale and nanoscale XRF and WAXS for that specific time-point.

** MicroCT and histology of all time points included healthy cortex (no extra samples were prepared).

the Lund Biolmaging Center (LBIC) using a MI Labs microCT device (MI Labs, Netherlands). MicroCT images were acquired in the ultra-focus mode at 65 kV voltage and 0.13 mA current using a primary Al 100 μm filter and a secondary Al 400 μm filter. 1440 projections with 90 ms ($n = 9$) and 120 ms ($n = 10$) exposure time were acquired over 360° . All tomograms were reconstructed using the manufacturers software suite to an isotropic voxel size of 10 μm , and later aligned and resliced along the longitudinal axis with DataViewer (V 1.4, Bruker, Germany). Additionally, bone phantoms with known 0.25 and 0.75 mg/mm^3 bone mineral density (BMD) were imaged for both sets of acquisition parameters to allow BMD calibration and quantification.

Regions of interest (ROI) were defined as ± 1.5 mm proximal and distal to the fracture line allowing for consistent volume evaluation across all samples. Bone volume was analyzed as highly mineralized tissue volume ($\text{BMD} > 0.642 \text{ mg}/\text{mm}^3$), and poorly mineralized tissue volume ($0.41 \text{ mg}/\text{mm}^3 < \text{BMD} < 0.642 \text{ mg}/\text{mm}^3$) based on literature [9,34]. This separation allowed for a more defined tracking of the callus mineralization process across time. Bone volume within the defined ROI was obtained from custom in-house MATLAB scripts (R2020b, The Mathworks Inc., U.S.).

2.3. Sample preparation

After microCT imaging, femurs to be analyzed with synchrotron techniques ($n = 9$, see Table 1) were fixed in neutral buffered formalin (4 % w/v) for 24 h, embedded in PMMA, split longitudinally in half, and later sectioned at appropriate thicknesses as described in the following subsections. A description of all the experimental parameters used in synchrotron techniques can be found in Supplementary Table 1. Samples for histology and immunohistochemistry were also fixed in formalin ($n = 10$, see Table 1) for 24 h followed by decalcification in 10% w/v EDTA for a period of 6-weeks with two EDTA changes every week. Decalcified samples were embedded in paraffin and cut to a thickness of 5 μm . Unless otherwise stated, all sectioning was performed using semi-automatic microtome (HM355S, Thermo Fisher Scientific, MA, USA).

2.4. Small-angle X-ray scattering

For SAXS measurements, PMMA-embedded healing femurs ($n = 3$, see Table 1) were sawed at a thickness between 130–240 μm using a precision cut-off machine (Accutom-100, Struers SAS,

France) with a silicon-carbide cut-off wheel (10S15, Struers SAS, France). Sections were then placed on aluminum sample holders. The experiments took place at the cSAXS beamline (Swiss Light Source, Switzerland) [35], where a section for each days-10, -14 and -21, were measured with an x-ray energy of 12.4 keV, a spot size of $50 \times 40 \mu\text{m}^2$, a step size of $50 \times 50 \mu\text{m}^2$ and an exposure time of 30 ms. The SAXS detector (Pilatus 2M, Dectris, Switzerland) was placed within a 7 m flight tube at 7095.6 mm from the sections. The sample detector distance and beam center were determined using a silver behenate powder standard.

The SAXS analysis was carried out with custom in-house MATLAB scripts [27,29,30], according to the model developed by B nger et al [24]. Recorded SAXS patterns were integrated azimuthally to highlight the anisotropic scattering coming from the preferential orientation of HA crystals. The two peaks 180° apart were fitted with gaussian curves above a background contribution. The crystal orientation was then compared to the crystallographic c-axis where a ratio between the anisotropic scattering and total scattering provides a scale of 0 - 1 of the degree of orientation (where 1 is highly aligned). HA crystal thickness (T-parameter) was quantified from the radially integrated patterns. Within the q-range $0.32 - 1.40 \text{ nm}^{-1}$, the scattering is assumed to be dominated by HA crystals under the assumption that these are platelets of finite thickness [24]. The T-parameter was calculated through iterative non-linear least squares fitting of this q-range for each scattered pattern, yielding dimensions between 0 - 3 nm [27].

2.5. Microscale X-ray fluorescence and wide-angle X-ray scattering

PMMA-embedded healing femurs ($n = 5$) were sectioned at $\sim 2\text{--}3 \mu\text{m}$ thickness and placed on Si_3N_4 windows ($1 \times 1 \text{ mm}^2$ membrane size, $1 \mu\text{m}$ membrane thickness, ref 1191118, Silson Ltd, UK). A sample was prepared for every time point, including a reference sample of the healthy cortex.

Simultaneous synchrotron-based scanning XRF and WAXS measurements were performed at the microXAS beamline (Swiss Light Source, Switzerland) [36]. Using an x-ray energy of 16.2 keV, 4 XRF single-element silicon drift detectors (Ketec GmbH, Germany) coupled to FalconX pulse processors (XIA LLC, USA) were placed 20 mm from the sample position at respective angles of 53° (front-left), 58° (front-right), 54° (back-left) and 60° (back-right) with respect to the beam path. Moreover, the WAXS detector (Eiger 4M, Dectris, Switzerland) was placed 130 mm behind the sample position.

In all sections ($n = 6$: days 7, 10, 14, 21 and 28, cortical bone), an initial overview XRF scan with a $2 \mu\text{m}$ beam focus, $10 \mu\text{m}$ step size and 100 ms dwell time, was acquired to determine the region of interest to be targeted at higher resolution. Once selected, these ROIs were acquired with a $1 \mu\text{m}$ beam focus and step size, and 100 ms dwell time. With the same parameters, LaB_6 was scanned as WAXS calibration standard and an empty window for background calibration.

XRF data was fitted using PyMCA [37]. The same software was used to generate Ca and Zn elemental maps, which were later stitched and analyzed using in-house Python and MATLAB scripts. Elemental maps were overlaid to compare their spatial distributions and relationship to WAXS analysis.

WAXS data calibration and azimuthal integration was achieved with PyFAI [38]. Crystallinity was defined in relation to the width Δ of the peaks corresponding to the [002] and [310] reflections, which are related to the length (L-parameter) and width (W-parameter) of coherent HA crystal blocks, respectively [29,39]. The fitting of these peaks and calculation of the respective L- and W-parameters was obtained with in-house MATLAB scripts by applying the Scherrer equation to the acquired datasets, after a 4×4 pixels

binning:

$$D = \frac{K\lambda}{\beta \cos \theta} \quad (1)$$

where D corresponds to the average crystal dimension corresponding to the analyzed reflection, K is the shape factor commonly set to 0.9 [29], λ the x-ray wavelength, β the full-width at half-maximum of the peak, and θ the scattering or Bragg angle.

To assess the relationship between the presence of Ca and/or Zn, and HA maturation, WAXS curves were averaged over different ROIs ($25 \times 25 \mu\text{m}^2$) corresponding to high-Ca low-Zn, high-Ca high-Zn, and low-Ca high-Zn. These curves were then qualitatively compared to understand how the spatial distribution of these elements relates to crystalline structures.

2.6. Nanoscale X-ray fluorescence and wide-angle X-ray scattering

PMMA-embedded healing femurs ($n = 5$) were sectioned at $\sim 2\text{--}3 \mu\text{m}$ thickness and placed on Si_3N_4 windows ($1 \times 1 \text{ mm}^2$ membrane size, $1 \mu\text{m}$ membrane thickness, ref 1191118, Silson Ltd, UK). Sections for days 7, 10 and 21 were the same as in microscale measurements, while different sections were used for the remaining days and healthy cortex. Moreover, a Si_3N_4 window with HA powder ($10 \mu\text{m}$ microparticles, Sigma Aldrich, Merck KGaA, Germany) was prepared as additional reference sample.

Simultaneous synchrotron-based scanning nano-XRF and WAXS measurements were performed at the NanoMAX beamline (MAX IV Laboratory, Sweden) [40,41]. With an x-ray energy of 12 keV, the XRF detector – single-element silicon drift detector (RaySpec, UK) coupled to an Xspress 3 pulse processor (Quantum Detectors, UK) – was placed 20 mm from the sample. The sections were placed perpendicular to the beam path, while the XRF detector was oriented at 30° with respect to the section. In addition, the WAXS detector (Pilatus 1M, Dectris, Switzerland) was placed 180 mm behind the sample. The ROIs were determined through an optical microscope mounted on-axis along the beam path.

All sections ($n = 7$: days 7, 10, 14, 21 and 28, cortical bone, HA microparticles) were scanned with a 75 nm beam focus, 100 nm step size and 100 ms dwell time. Moreover, an RF-C0 thin film (AXO Dresden GmbH, Germany) and a Si film were acquired as XRF and WAXS calibration standards, respectively. An empty Si_3N_4 window was scanned for background calibration. Due to the higher sample thickness ($\sim 2\text{--}3 \mu\text{m}$) in comparison to the spot size (75 nm), the spatial resolution is lower than the spot size. However, a certain slice thickness is required to achieve enough signal for measurement and analysis.

Calibration, fitting, and generation of elemental maps were obtained with PyMCA. Ca, Zn and Fe concentration maps were overlaid to compare their spatial distributions. WAXS data was calibrated and azimuthally integrated using PyFAI. As previously explained in Section 2.5, crystallinity was assessed through estimation of the L- and W-parameters corresponding to the [002] and [310] reflections (see Equation 1). Mean and standard deviation of these parameters were computed for each time-point, cortex and HA microparticles over the whole datasets.

With the aim to correlate elemental distribution with the [002] and [310] reflections, ROIs were placed and analyzed across mineralized areas undergoing remodelling in days-14, -21 and -28. The ROIs had a fix size of $1 \times 4 \mu\text{m}^2$, starting at the mineralization edge and going deeper into more mature mineralized tissue. Elemental concentrations (normalized by the maximum individual concentrations within the ROI) and WAXS curves were averaged over the short axis ($1 \mu\text{m}$, 10 pixels) and presented with respect to the depth of the ROI ($4 \mu\text{m}$, 40 pixels) as line profiles and surfaces, respectively. A detailed representation of these ROIs can be found in section 3.2 of the Results.

2.7. Histology analysis with Safranin O/fast green

Sections collected from each time point (day 7, 10, 14, 21 and 28, $n = 2$ per time point) were stained with safranin O/fast green, which stains cytoplasm and collagen green/blue, and proteoglycans red. Tissue sections were deparaffinized using xylene and rehydrated using decreasing ethanol gradient and water. Hydrated tissue sections were placed in 0.1% (w/v) fast green solution for 10 min followed by a dip in 1% (v/v) acetic acid. Slides were then moved to a jar containing 0.1% (w/v) safranin O for 5 min following which the slides were dehydrated using increasing ethanol gradient and cleared in xylene. Slides were allowed to dry for 5 min after which they were mounted using a xylene based mounting medium.

2.8. Immunohistochemistry analysis of spatial distribution of MMP-13

MMP-13 staining was performed on sections from each time point (day 7, 10, 14, 21 and 28, $n = 2$ per time point). Briefly, all the slides were placed in 37°C for 48 h and then deparaffinized (xylene) and rehydrated (decreasing ethanol gradient followed by water). Pepsin (ab64201, Abcam, U.K) was used to achieve antigen retrieval for 30 min at 37°C. Hydrogen peroxide blocking reagent (ab64218, Abcam, U.K) was used to inactivate the endogenous peroxidase for 8 min. 0.2% Bovine testicular Hyaluronidase (H3506) was used in conjunction with collagenase to improve the extracellular matrix penetration of the antibody for 30 min. Protein Block was then used for 30 min to block non-specific antibody binding sites. The slides were incubated with anti-MMP-13 (ab219620, Abcam, U.K, dilution 1:200) antibody overnight in humidified chamber at 4°C. Subsequently, secondary antibody (goat anti-rabbit IgG-HRP conjugated, ab205718, Abcam, U.K) was applied at 1:200 dilution for 60 min at room temperature. The color developing DAB solution (ab64238) was added and incubated for 30 min with constant monitoring under a microscope. Lastly, hematoxylin (ab220365) was added to the slides for 10 s. The slides were then dehydrated, cleared in xylene and mounted using a xylene based mounting medium. For immunohistochemistry staining, only secondary antibody staining with the above steps were done to avoid false positive stains and confirm the reliability of antibody-based staining.

2.9. Statistical analysis

The data is presented as average and standard deviation, both for intra- and inter-sample comparison. Due to the low number of samples per time-point, no further statistical analyses were performed.

3. Results

3.1. Macroscale visualization and confirmation of in-vivo long bone fracture healing model

The progressive stages of long bone fracture healing can clearly be identified from microCT scans and Safranin O/Fast green histology (Fig. 2). The expected progressive mineralization starts at the pre-existing cortex building out to a bony wedge on top of the cartilaginous callus. Subsequently, the mineralization progresses outwards and bridging of the callus occurs. Quantification of the 3D bone formation (see Supplementary Table 2 and Supplementary Fig. 1) shows an increase of total callus volume (TCV) over time until it clearly peaks at day 21, to later reduce until day 28, when the healing process has been almost completed. This is mainly driven by the low mineralized bone volume (LMBV), which follows

the same pattern. Instead, high mineralized bone volume (HMBV) remains constant between days 7–14, and then it starts increasing at days 21–28 due to the mineralization of the cartilaginous tissue.

3.2. Multi-scale elemental and structural characterization

From the low resolution SAXS analysis (see Supplementary Fig. 2), the mineral crystal thickness (T-parameter) follows mineralization by increasing 3–4-fold from the mineralization front into the mature callus, and 6–7-fold from the mineralization front into the cortical bone. The degree of orientation within the callus tissue remains at ~ 0.55 throughout the different time-points, which represents less well oriented bone compared to cortical bone (~ 0.6 – 0.7), as previously reported by Mathavan et al. [42].

The relationship between elemental distributions and HA dimensions at the mineralization front across healing time-points were further studied with higher resolution (Figs. 3–5). In the microscale XRF images (Fig. 3), the mineralization front begins with high-Zn low-Ca areas followed by an increase of Ca, which points to initial mineralization. Later, more mature regions are also characterized by an increase of Zn, especially at the edges of high-Ca structures as well as in the bulk. The corresponding WAXS data from mineralization front regions with a high-Zn low-Ca distribution show that, at this stage, HA may either not yet be crystalline, or the amount is below detection limits (flat curves). Crystal peaks appear in more mature regions deeper in the bulk and increase with healing time until they approach cortical reference values. Remodeling regions with high-Ca high-Zn distribution show either very high crystallinity when located in the mineral bulk (day-14), or lower crystallinity when located at the edges (day-21), which indicates that mineral deposition or resorption is taking place.

The HA crystal dimensions (L- and W-parameters) progress towards cortical values across healing time-points (Supplementary Fig. 3). The most noticeable progression, especially in terms of W-parameter, is found towards the end of the healing process, between days 21 and 28. Due to the resolution used, it is difficult to interpret spatial correlations of these values. Also noticeable are the large regional variabilities within each map, which indicate that different parts of the callus present either endochondral mineralization, remodeling of existing mineralized tissue or bulk matured HA.

The nanoscale XRF measurements show that mineralization begins with high-Zn low-Ca content, while Ca increases in more mature regions until Zn appears again at the edges of mature structures, specially starting at day-14 (Fig. 4). Consistently, also starting at the same healing time, high-Fe concentrations are located at the edges of Zn. Average mineral crystal length and width (L- and W-parameters) show a slight increase with healing time towards the highest values found in cortical bone and HA microparticles (Supplementary Fig. 4).

The relationship between the distributions of Ca, Zn, Fe and bone remodeling processes was further explored at the edge of the mineralized tissue (Fig. 5). In every time-point, WAXS peaks are progressively formed starting from the edges, where Zn and Fe are high, but Ca remains low. At day-14, Fe concentration shows a very clear initial peak and sharp decrease, followed by a Zn peak and a gradual increase of Ca. This order of events is consistently found in all time-points, while the clear Fe and Zn peaks turn into 'plateaus' at increasing time points as the tissue matures towards cortical bone.

Similar to the micro-scale counterpart, the nano-scale WAXS data shows that the HA crystal length and width (L- and W-parameters) increase over healing time towards the values found in the cortical bone references (Supplementary Fig. 4). L-parameter values show a slight gradient in which the crystals at the mineralization front are longer than the ones in bulk in regions, while

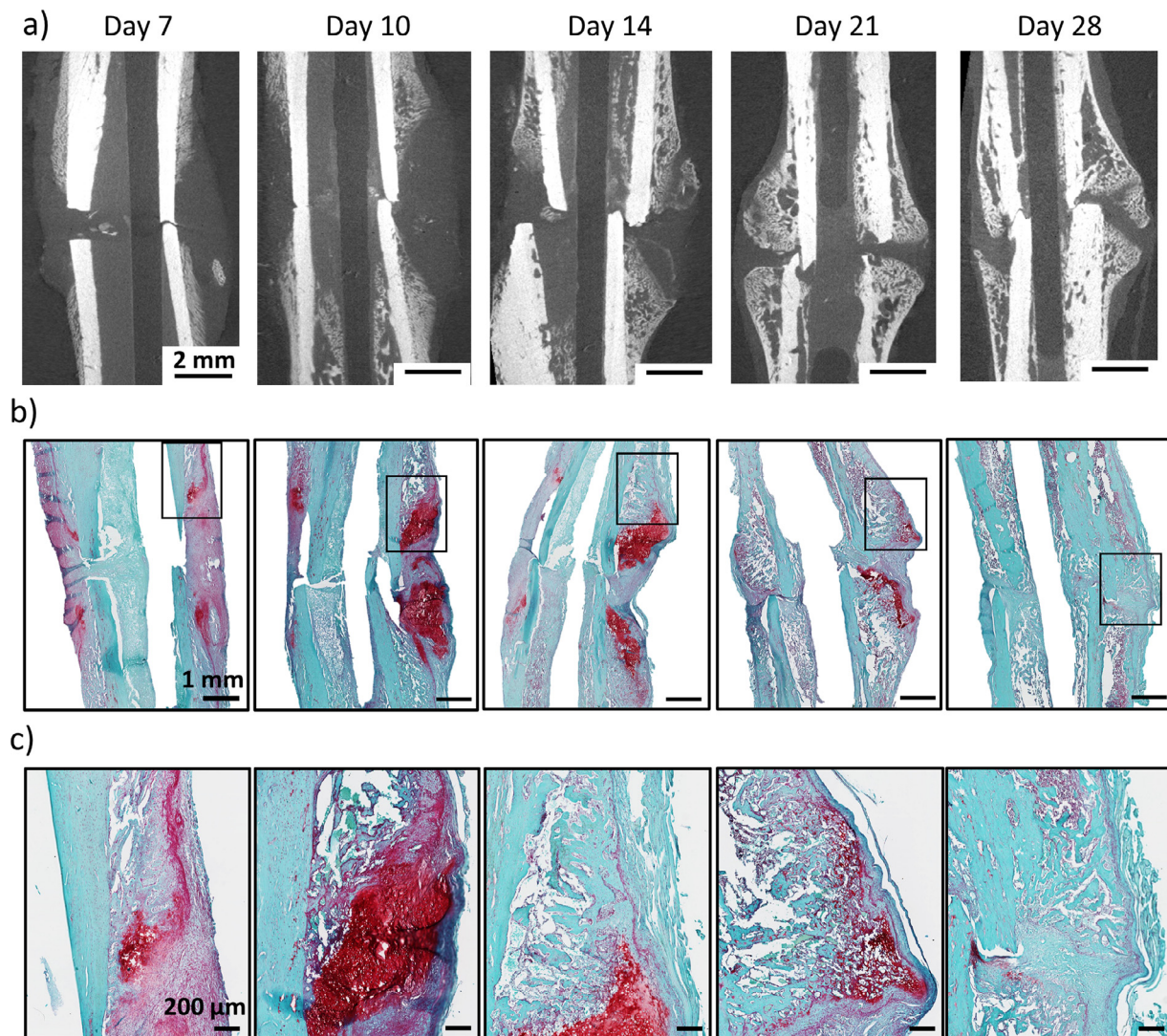


Fig. 2. Representative microCT slices for each of the investigated time-points. b) SaO/Fast green section of approximately the same location as in a). The rectangles mark the zoomed in regions shown in c). In b) and c), red stains for cartilaginous tissue and blue/green for other mineralized and non-mineralized tissues. Scale bars in a), b) and c) are 2 mm, 1 mm and 200 μm, respectively.

the W-parameter clearly shows lower values (thinner crystals) at both the mineralization front and remodeling regions in mineralized patches. These results point towards HA maturation processes during mineralization.

3.3. Distribution of MMP-13 expression in mineralizing callus

In general, the intensity of MMP-13 expression follows a clear trend with increased expression early on, peaking at day 10, which gradually decreases over time and is almost absent at day 28 (Fig. 6). At the early time points (day 7 and 10), MMP-13 staining is observed at the interface of the bone and cartilage tissue indicating progressive degradation and mineralization of the cartilage matrix. MMP-13 expression at these two time points can only be observed in chondrocyte like cells. With the passage of time, as the clear distinction between bone and cartilage tissue becomes less prominent, MMP-13 expression is observed both in the cartilage matrix as well as in the trabecular islands formed within the callus tissue. This is more prominent at days 14 and 21. At day 28, faint expression of MMP-13 can be observed in the mineralized callus, which is markedly different to what is observed at days 7 and 10.

4. Discussion

In this study, we progressively followed the mineralization front in an *in-vivo* long bone fracture healing model [9], from the first deposition of Ca to the mineralization and development of mature HA crystals. In these regions, elemental and structural characterization of the forming bone was investigated based on a multi-modal multi-scale approach by combining low resolution microCT and SAXS mapping, with higher resolution (microscale and nanoscale) synchrotron-based scanning XRF and WAXS, and immunohistochemistry. To our knowledge, this is the first time that such a range of techniques probing different length-scales and mineralization constituents has been applied to investigate bone formation during fracture healing. Specifically, performing nanoscale measurements allowed us to achieve a comprehensive understanding of the underlying mineralization processes.

Through microCT imaging of the healing femurs, it was possible to visualize and quantify the global morphological changes along the healing process in the utilized *in-vivo* model. In accordance with the literature [9,11–13], a soft cartilaginous callus started forming in the early stages (days-7, 10), which was seen

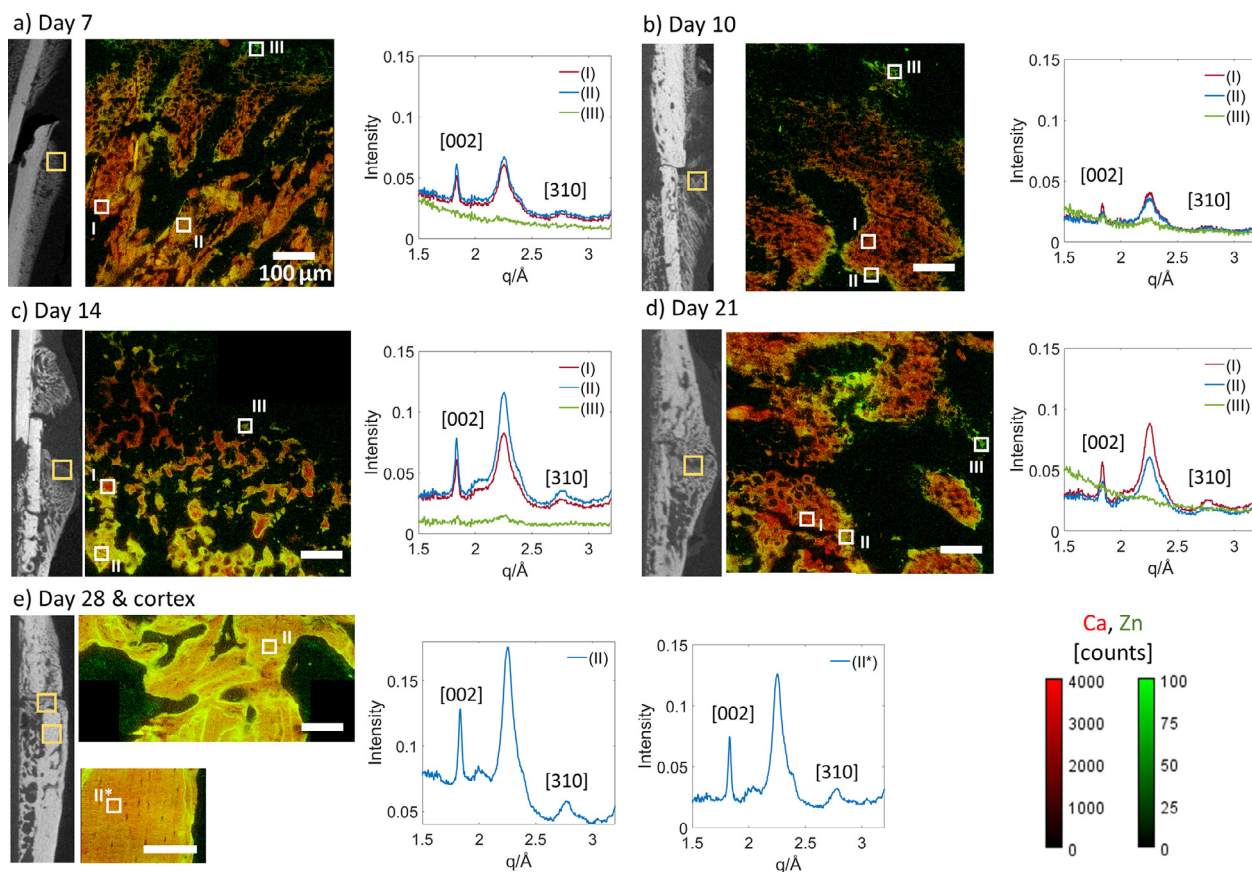


Fig. 3. Relationship between Ca-Zn distribution and HA crystal maturity in microscale XRF and WAXS. For every time point (a-e) and a cortical bone reference (e), a microCT image shows the approximate location of the section analyzed with microscale XRF and WAXS. Ca-Zn maps (red-green) of these locations are shown with ROIs corresponding to high-Ca low-Zn (I), high-Ca high-Zn (II) and low-Ca high-Zn (III) regions. The average WAXS curves for these ROIs (I-III) are plotted to show the crystallinity in each of these characteristic regions (I – red, II – blue, III – green). The scale bar in each XRF image is 100 μm .

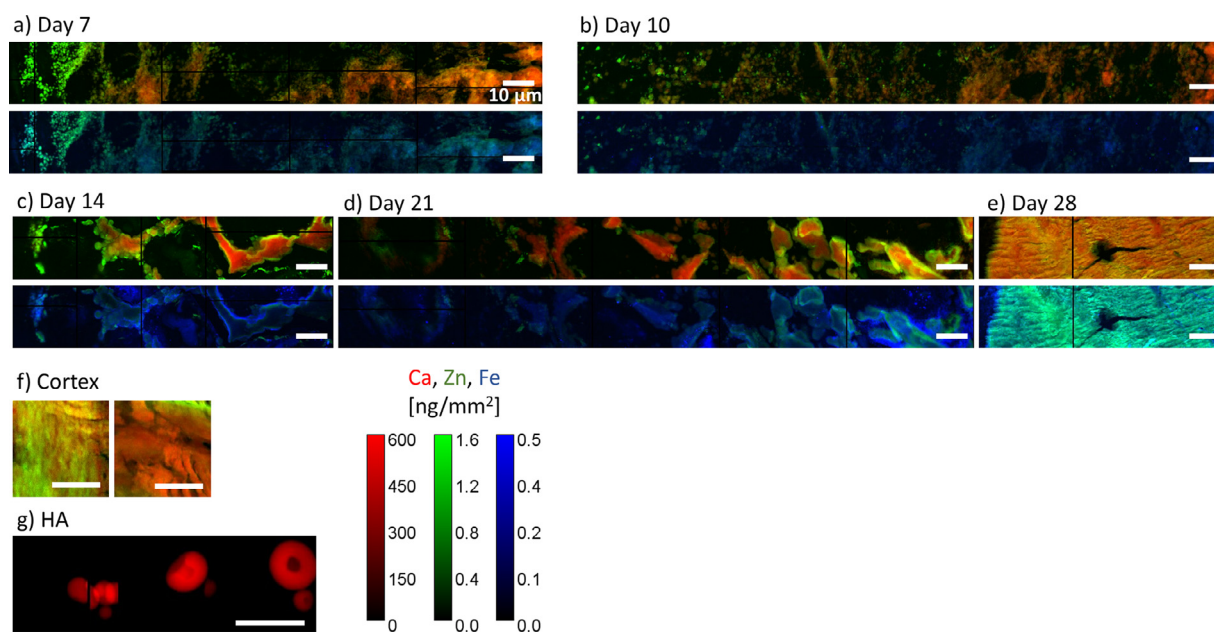


Fig. 4. Nano-XRF maps of Ca-Zn (red-green) and Zn-Fe (green-blue) of the mineralization front for days (a) 7, (b) 10, (c) 14, (d) 21 and (e) 28. The mineralization front is located on the left side of the images. (f) Ca-Zn map for cortical bone references and (g) Ca map for HA microparticles reference. Blue, yellow and green represent data from mineralization front (a-e), cortical bone references (f) and HA microparticles (g), respectively. The scale bar in each XRF image is 10 μm .

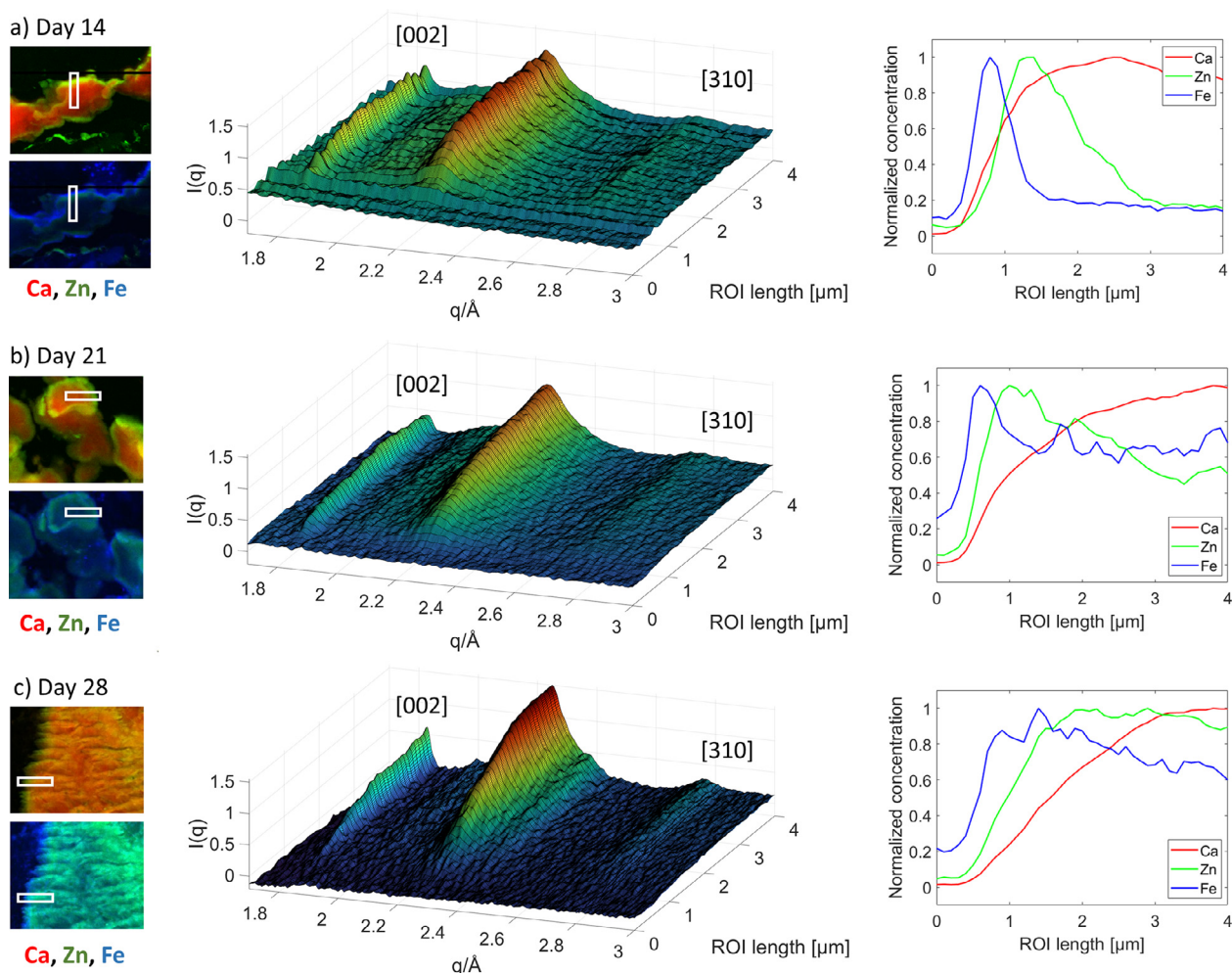


Fig. 5. Relationship between HA maturation and Ca, Zn, Fe normalized concentration across edges of mineralized tissue at days (a) 14, (b) 21 and (c) 28. For each time-point, the left column shows nano-XRF images with the analyzed ROIs (white rectangles, $1 \times 4 \mu\text{m}^2$) across the edge of mineralized tissue. The middle column shows the average WAXS curves along the ROI's length (mineralized tissue depth) as a surface, while the right column includes plots of Ca, Zn and Fe concentrations (normalized to individual maximum within the ROI) along the corresponding ROI's length.

fully grown and progressively mineralized (days-14, 21) until rejoining the cortical bone at the fracture line (days-21, 28). Finally, the mineralized callus started to remodel, which over time will resorb the callus aiming to recover the original bone properties and morphology. This final process can take months to years to be completed [11,43].

With the combination of synchrotron based high-resolution XRF and WAXS techniques (Figs. 3–5), we were able to relate the distributions of Ca, Zn and Fe, to the deposition and maturation of HA. By combining these techniques at the micro- and nanoscale it was possible to first achieve measurements over large areas of interest ($\sim 600 \times 600 \mu\text{m}^2$) going deep into the fracture region with micrometer resolution, and then target the very mineralization front and achieve nanoscale resolution and high sensitivity in smaller areas of interest at the most active regions ($\sim 20 \times 100 \mu\text{m}^2$). Therefore, this multiscale approach allowed a more comprehensive and complete assessment of the fracture healing site. Through these measurements, increased Zn and low Ca concentrations were observed at the mineralization front surrounding hypertrophic chondrocytes, where endochondral ossification takes place via new deposition of CaP. In addition, high Zn was also detected in remodeling sites of more mature regions. These findings suggest that Zn is not only related to new mineral deposition, but to the resorption processes during callus remodeling as well. The XRF findings

were further supported by the presented WAXS data, which indicated initial mineralization at the front, while progressive crystalline peaks were present in the remodeling regions. The observation of such spatial distribution of Zn is in agreement with previous findings in embryonic mice bone development and in the limbs of 10-day old rats [30,44]. Additionally, high-Zn concentration has been reported in equine and human bone-cartilage interface [44–47] or human osteosarcoma [48], which indicates that elevated levels of Zn are predominant in diverse metabolically active regions. Our results confirmed that Zn plays a key role in mineralization overall, including intramembranous and endochondral ossification. The reasons for the localized increased Zn concentrations may be multiple. Zn has been reported to act as a co-factor for different MMPs and alkaline phosphatase, including MMP-13, which is expressed by the aforementioned hypertrophic chondrocytes and osteoblasts in the mineralization front [1,49–51]. Moreover, Zn has been reported to substitute Ca within HA during intracellular nucleation processes in an *in-vitro* study [4]. At the cellular level, human mesenchymal stem cells (hMSCs) cultured on Zn substrates exhibited significantly better osteogenic differentiation potential with respect to the controls [52]. The data shown in our study represented a combination of these and potentially other Zn functions. Notably, Zn appeared in the form of small concentrates at the mineralization front across all time-points, but es-

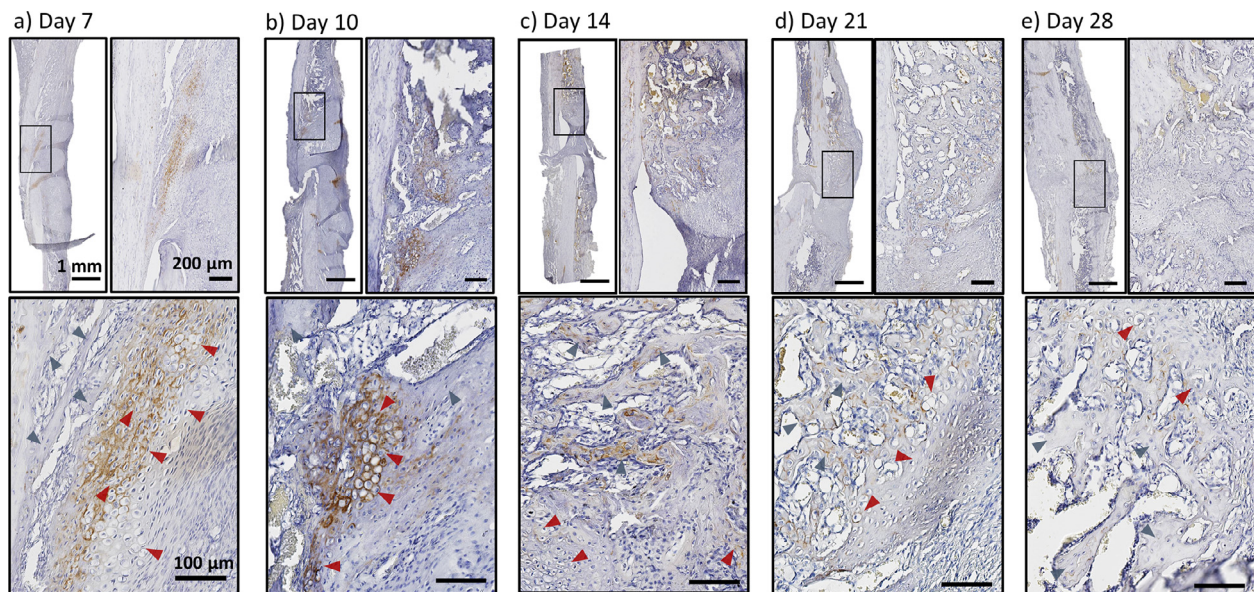


Fig. 6. MMP-13 immunohistochemical staining of the specimens from the fracture healing study at different healing stages. For each time point, top left provides a low magnification overview of the entire fracture callus from one side. Top right presents a magnified region (magnification: 5X) showing the interface between the mineralized and non-mineralized regions with prominent MMP-13 staining. Bottom shows a highly magnified region (magnification: 20X) emphasizing on the cellular composition of the MMP-13 positive tissue. Brown regions indicate MMP-13 positive cells and extracellular matrix. Sections were counterstained with hematoxylin. Scale bar: top left= 1 mm, top right= 200 μ m, bottom= 100 μ m. Red arrow heads indicate cartilage tissue while grey arrow heads indicate bone tissue.

pecially at the earlier time-points (days-7, -10, see Fig. 4), which could be indicative of nucleation sites or the presence of matrix vesicles, which are released by osteoblasts and chondrocytes to initiate calcification [53], or simply because the mineralization rate is substantially higher during these time points [9]. In the remodeling sites, Zn instead appeared to surround the periphery of the trabecular islands, and is suggested to play an anti-catabolic role by reducing osteoclastogenesis via the inhibition of NF- κ B signaling pathway [54].

The high resolution achieved with nano-XRF allowed to probe elemental distribution and HA maturation changes at 10 times lower scale than the micro-scale data, thus becoming much more sensitive to detailed variations at the mineralization front. Interestingly, this resulted in the novel observation of a characteristic distribution of Fe across time-points (see Figs. 4 and 5), which has not been reported before. At early time-points (days-7, 10), Fe was uniformly distributed throughout the mineralizing callus. Nevertheless, at later time-points (days-14, 21), thin regions with high Fe concentration appeared surrounding the edges of high Zn areas. This suggests that Fe acts earlier than and in coordination with Zn during mineralization. This can be clearly visualized in Fig. 5 (right column), where the profile plots of normalized Ca, Zn and Fe concentrations showed a very first peak of Fe followed by a peak of Zn, while Ca progressively increased along these two. The available literature tackling the relationship between Fe and mineralization is rather scarce. The spatio-temporal distribution pattern of Fe in our study could partly indicate neo-vascularization of the cartilage template since one of the hallmarks of endochondral ossification is the formation of a vascularized cartilage matrix, which is followed by hypertrophy and eventual mineralization [12]. Alternatively, as reviewed by Medeiros et al. [55], other studies focused on the effects of dietary restriction and found that Fe deficiency in rats is correlated to bone fragility, compromised bone microarchitecture and turnover, reduced matrix formation and reduced *in-vitro* mineralization of osteoblasts [56–59]. Fe is a component of prolyl hydroxylases converting proline to hydroxyproline, which is required for collagen crosslinking [18]. Therefore, these studies speculated that a poor collagen deposition and turnover is the cause of such

findings. Applied to fracture healing, the reported distribution of Fe might have indicated an initial deposition of collagen, which was later mineralized through the function of Zn as MMP co-factor. To our knowledge, this is the first time such a spatial distribution of Fe in relation to mineralization has been reported. Nevertheless, these hypotheses compel further investigation before the role of Fe can be better established in the mineralization process during long bone healing.

Since MMP-13 contains Zn in its catalytic domain and participates in collagen type II turnover [32,60], we aimed to compare the spatial distribution of MMP-13 distribution via immunohistochemistry with the elemental distribution discussed above. As expected, MMP-13 was found around hypertrophic chondrocytes at the mineralization front, especially in the early healing process. During the later time-points, despite a reduction in the MMP-13 expression which potentially indicated reduced collagen type II remodeling, MMP-13 was still found to be concentrated at specific sites around the mineralized regions. As these measurements were performed in different tissue slices, exact co-location was not possible. However, MMP-13 results seemed to generally correlate well with the spatial distribution of Zn as obtained by XRF techniques (Fig. 7a–c). In day-28 and cortical bone, MMP-13 signal was not prominent even when high Zn concentrations were observed throughout the tissue in XRF data. This indicates that in bone undergoing remodeling, which mainly comprises of collagen type I, Zn could be related to other processes involving homeostasis. To fully confirm the spatial correlation between MMP-13 and Zn further studies of co-location in the same samples using consecutive sections would be required. This was unfortunately not possible, as the preparation protocols for the techniques used in this study are vastly different.

The main limitations of this study were related to the use of synchrotron and 2D imaging techniques. There is a high demand and low availability of experimental time in synchrotrons, while the experimental techniques are time intensive. This leads to the measurement of limited amounts of samples and rather small ROI dimensions. Keeping that in mind, our goal was to investigate at least 1 sample per healing time-point, while maximizing the scanned area in each of them. In addition, some of the presented

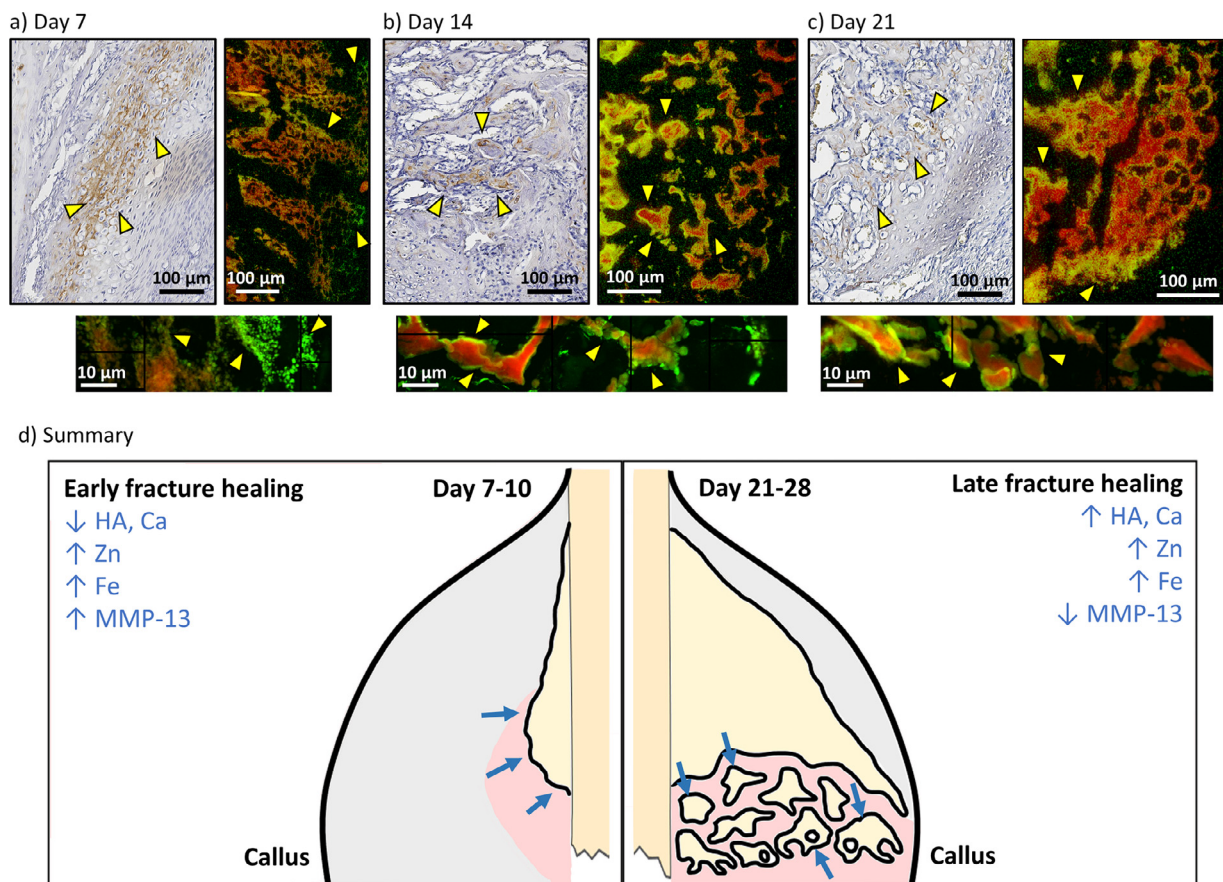


Fig. 7. Spatio-temporal correlation of MMP-13 with Ca and Zn. MMP-13 immunochemistry (first row, left), micro-XRF (first row, right) and nano-XRF (second row) of the mineralizing callus at days a) 7, b) 14 and c) 21. Brown indicates presence of MMP-13, red corresponds to Ca and green, to Zn. Yellow arrow heads indicate regions where Zn and MMP-13 appear to be correlated (observe that XRF and MMP-13 data was obtained from different rats). d) Graphical representation summarizing of the findings of this manuscript. Darker yellow stands for bone, lighter yellow for newly mineralized tissue, red for cartilage template, and gray for the rest of soft-tissue callus. Blue arrows indicate where Zn and MMP-13 appear to be correlated. (For interpretation of the references to colour in this figure legend, the reader is referred to the web version of this article.)

techniques (SAXS, XRF, WAXS, histology) are based on the preparation and imaging of 2D sections. While we used the microCT data to guide ourselves and select representative regions for slicing, these cannot fully describe the complexity of 3D structural features and might contain artefacts related to sample preparation procedures (folding, rupture), which were avoided during analysis. Additionally, formalin fixation has been reported to cause a loss of Ca and other trace elements prior to spectroscopic measurements [61,62]. However, all samples were prepared following the exact same protocol to minimize potential inter sample variations.

This study presented novel elemental and structural characterization of tissue mineralization in an *in-vivo* rat model of bone fracture healing using a multi-resolution multi-modal approach (Fig. 7d). For the first time to our knowledge, the spatio-temporal distribution of Ca, Zn, Fe and MMP-13 across time has been related to the initial mineral deposition and remodeling processes of mature regions. Even if the specific action mechanisms of these elements could not exactly be pinpointed, further understanding of the mechanisms involved can ultimately lead to targeted treatments enhancing new bone formation, e.g. during impaired bone healing.

Data availability statement

Data available on request from the authors.

Declaration of Competing Interest

DBR holds stocks in Moroxite AB, which is unrelated to this work. The authors declare no conflicts of interest.

Acknowledgements

We acknowledge the Lund BioImaging Center (LBIC) for microCT imaging; the Paul Scherrer Institut, Villigen, Switzerland for provision of synchrotron radiation beamtime at beamlines cSAXS (Proposal 20191767) and microXAS of the SLS (Proposal 20211780); and MAX IV Laboratory for time on beamline NanoMAX (Proposals 20190849 & 20210697). Research conducted at MAX IV, a Swedish national user facility, is supported by the Swedish Research council under contract 2018-07152, the Swedish Governmental Agency for Innovation Systems under contract 2018-04969, and Formas under contract 2019-02496. Funding from the Knut and Alice Wallenberg Foundation (Wallenberg Academy Fellows 2017.022) is acknowledged.

Supplementary materials

Supplementary material associated with this article can be found, in the online version, at [doi:10.1016/j.actbio.2023.06.031](https://doi.org/10.1016/j.actbio.2023.06.031).

References

- [1] N. Ortega, D.J. Behonick, Z. Werb, Matrix remodeling during endochondral ossification, *Trends Cell Biol.* 14 (2004) 86–93, doi:[10.1016/j.tcb.2003.12.003](https://doi.org/10.1016/j.tcb.2003.12.003).
- [2] E.J. Mackie, Y.A. Ahmed, L. Tatarczuch, K.S. Chen, M. Mirams, Endochondral ossification: How cartilage is converted into bone in the developing skeleton, *Int. J. Biochem. Cell Biol.* 40 (2008) 46–62, doi:[10.1016/j.biocel.2007.06.009](https://doi.org/10.1016/j.biocel.2007.06.009).
- [3] A. Lotsari, A.K. Rajasekharan, M. Halvarsson, M. Andersson, Transformation of amorphous calcium phosphate to bone-like apatite, *Nat. Commun.* 9 (2018), doi:[10.1038/s41467-018-06570-x](https://doi.org/10.1038/s41467-018-06570-x).
- [4] A. Procopio, E. Malucelli, A. Pacureanu, C. Cappadone, G. Farruggia, A. Sargenti, S. Castiglioni, D. Altamura, A. Sorrentino, C. Giannini, E. Pereira, P. Cloetens, J.A.M. Maier, S. Iotti, Chemical fingerprint of Zn-hydroxyapatite in the early stages of osteogenic differentiation, *ACS Cent. Sci.* 5 (2019) 1449–1460, <https://doi.org/10.1021/acscentsci.9b00509>.
- [5] B.M. Oosterlaken, M.P. Vena, G. de With, In vitro mineralization of collagen, *Adv. Mater.* (2021) 33, doi:[10.1002/adma.202004418](https://doi.org/10.1002/adma.202004418).
- [6] F. Nudelman, A.J. Lausch, N.A.J.M. Sommerdijk, E.D. Sone, In vitro models of collagen biomineralization, *J. Struct. Biol.* 183 (2013) 258–269, doi:[10.1016/j.jsb.2013.04.003](https://doi.org/10.1016/j.jsb.2013.04.003).
- [7] X. Luo, D. Barbieri, N. Davison, Y. Yan, J.D. De Bruijn, H. Yuan, Zinc in calcium phosphate mediates bone induction: In vitro and in vivo model, *Acta Biomater.* 10 (2014) 477–485, doi:[10.1016/j.actbio.2013.10.011](https://doi.org/10.1016/j.actbio.2013.10.011).
- [8] Y. Ling, H.F. Rios, E.R. Myers, Y. Lu, J.Q. Feng, A.L. Boskey, DMP1 depletion decreases bone mineralization in vivo: an FTIR imaging analysis, *J. Bone Miner. Res.* 20 (2005) 2169–2177, doi:[10.1359/jbmr.050815](https://doi.org/10.1359/jbmr.050815).
- [9] N. Mathavan, P. Bosemark, H. Isaksson, M. Tägil, Investigating the synergistic efficacy of BMP-7 and zoledronate on bone allografts using an open rat osteotomy model, *Bone* 56 (2013) 440–448, doi:[10.1016/j.bone.2013.06.030](https://doi.org/10.1016/j.bone.2013.06.030).
- [10] A. Vortkamp, S. Pathi, G.M. Peretti, E.M. Caruso, D.J. Zaleske, C.J. Tabin, Recapitulation of signals regulating embryonic bone formation during postnatal growth and in fracture repair, *Mech. Dev.* 71 (1998) 65–76, doi:[10.1016/S0925-4773\(97\)00203-7](https://doi.org/10.1016/S0925-4773(97)00203-7).
- [11] R. Marsell, T.A. Einhorn, The biology of fracture healing, *Injury* 42 (2011) 551–555, doi:[10.1016/j.injury.2011.03.031](https://doi.org/10.1016/j.injury.2011.03.031).
- [12] T.A. Einhorn, L.C. Gerstenfeld, Fracture healing : mechanisms and interventions, *Nat. Publ. Gr.* 11 (2015) 45–54, doi:[10.1038/nrrheum.2014.164](https://doi.org/10.1038/nrrheum.2014.164).
- [13] L.C. Gerstenfeld, D.M. Cullinane, G.L. Barnes, D.T. Graves, T.A. Einhorn, Fracture healing as a post-natal developmental process: Molecular, spatial, and temporal aspects of its regulation, *J. Cell. Biochem.* 88 (2003) 873–884, doi:[10.1002/jcb.10435](https://doi.org/10.1002/jcb.10435).
- [14] N. Kosaki, H. Takaishi, S. Kamekura, T. Kimura, Y. Okada, L. Minqi, N. Amizuka, U. il Chung, K. Nakamura, H. Kawaguchi, Y. Toyama, J. D'Armiento, Impaired bone fracture healing in matrix metalloproteinase-13 deficient mice, *Biochem. Biophys. Res. Commun.* 354 (2007) 846–851, doi:[10.1016/j.bbrc.2006.12.234](https://doi.org/10.1016/j.bbrc.2006.12.234).
- [15] M. Inada, Y. Wang, M.H. Byrne, M.U. Rahman, C. Miyaura, C. López-Otin, S.M. Krane, Critical roles for collagenase-3 (Mmp13) in development of growth plate cartilage and in endochondral ossification, *Proc. Natl. Acad. Sci. U. S. A.* 101 (2004) 17192–17197, doi:[10.1073/pnas.0407788101](https://doi.org/10.1073/pnas.0407788101).
- [16] B. Pemmer, A. Roschger, A. Wastl, J.G. Hofstaetter, P. Wobraschek, R. Simon, H.W. Thaler, P. Roschger, K. Klaushofer, C. Strelj, Spatial distribution of the trace elements zinc, strontium and lead in human bone tissue, *Bone* 57 (2013) 184–193, doi:[10.1016/j.bone.2013.07.038](https://doi.org/10.1016/j.bone.2013.07.038).
- [17] K. Maciejewska, Z. Drzazga, M. Kaszuba, Role of trace elements (Zn, Sr, Fe) in bone development: Energy dispersive X-ray fluorescence study of rat bone and tooth tissue, *BioFactors* 40 (2014) 425–435, doi:[10.1002/biof.1163](https://doi.org/10.1002/biof.1163).
- [18] D.M. Medeiros, J. Ilich, J. Ireton, V. Matkovic, L. Shiry, R. Wildman, Femurs from rats fed diets deficient in copper or iron have decreased mechanical strength and altered mineral composition, *J. Trace Elem. Exp. Med.* 10 (1997) 197–203, doi:[10.1002/\(SICI\)1520-670X\(1997\)10:3<197::AID-JTRA7>3.0.CO;2-8](https://doi.org/10.1002/(SICI)1520-670X(1997)10:3<197::AID-JTRA7>3.0.CO;2-8).
- [19] M. Pierantoni, S. Le, V. Sotiriou, S. Ahmed, A.J. Bodey, I. Jerjen, N.C. Nowlan, H. Isaksson, D.L. Source, Muscular loading affects the 3D structure of both the mineralized rudiment and growth plate at early stages of bone formation, *Bone* 145 (2021) 115849, doi:[10.1016/j.bone.2021.115849](https://doi.org/10.1016/j.bone.2021.115849).
- [20] P. Suortti, B. Thomlinson, Medical applications of synchrotron radiation, *Synchrotron Radiat. News* 24 (2011) 2, doi:[10.1080/08940886.2011.567156](https://doi.org/10.1080/08940886.2011.567156).
- [21] F. Peyrin, Investigation of bone with synchrotron radiation imaging: From micro to nano, *Osteoporos. Int.* 20 (2009) 1057–1063, doi:[10.1007/s00198-009-0855-8](https://doi.org/10.1007/s00198-009-0855-8).
- [22] P. Fratzl, S. Schreiber, K. Klaushofer, Bone mineralization as studied by small-angle x-ray scattering, *Connect. Tissue Res.* 35 (1996) 9–16, doi:[10.3109/03008209609005268](https://doi.org/10.3109/03008209609005268).
- [23] S. Rinnerthaler, P. Roschger, H.F. Jakob, A. Nader, K. Klaushofer, P. Fratzl, Scanning small angle X-ray scattering analysis of human bone sections, *Calcif. Tissue Int.* 64 (1999) 422–429, doi:[10.1007/PL00005824](https://doi.org/10.1007/PL00005824).
- [24] M.H. Büniger, H. Oxlund, T.K. Hansen, S. Sørensen, B.M. Bibby, J.S. Thomsen, B.L. Langdahl, F. Besenbacher, J.S. Pedersen, H. Birkedal, Strontium and bone nanostructure in normal and ovariectomized rats investigated by scanning small-angle X-ray scattering, *Calcif. Tissue Int.* 86 (2010) 294–306, doi:[10.1007/s00223-010-9341-8](https://doi.org/10.1007/s00223-010-9341-8).
- [25] N. Mathavan, M.J. Turunen, M. Tägil, H. Isaksson, Characterising bone material composition and structure in the ovariectomized (OVX) rat model of osteoporosis, *Calcif. Tissue Int.* 97 (2015) 134–144, doi:[10.1007/s00223-015-9991-7](https://doi.org/10.1007/s00223-015-9991-7).
- [26] J.D. Kaspersen, M.J. Turunen, N. Mathavan, S. Lages, J.S. Pedersen, U. Olsson, H. Isaksson, Small-angle X-ray scattering demonstrates similar nanostructure in cortical bone from young adult animals of different species, *Calcif. Tissue Int.* 99 (2016) 76–87, doi:[10.1007/s00223-016-0120-z](https://doi.org/10.1007/s00223-016-0120-z).
- [27] M.J. Turunen, S. Lages, A. Labrador, U. Olsson, M. Tägil, J.S. Jurvelin, H. Isaksson, Evaluation of composition and mineral structure of callus tissue in rat femoral fracture, *J. Biomed. Opt.* 19 (2014) 025003, doi:[10.1117/1.jbo.19.2.025003](https://doi.org/10.1117/1.jbo.19.2.025003).
- [28] A.S. Acerbo, A.T. Kwaczala, L. Yang, S. Judex, L.M. Miller, Alterations in collagen and mineral nanostructure observed in osteoporosis and pharmaceutical treatments using simultaneous small- and wide-angle X-ray scattering, *Calcif. Tissue Int.* 95 (2014) 446–456, doi:[10.1007/s00223-014-9913-0](https://doi.org/10.1007/s00223-014-9913-0).
- [29] M.J. Turunen, J.D. Kaspersen, U. Olsson, M. Guizar-Sicairos, M. Bech, F. Schaff, M. Tägil, J.S. Jurvelin, H. Isaksson, Bone mineral crystal size and organization vary across mature rat bone cortex, *J. Struct. Biol.* 195 (2016) 337–344, doi:[10.1016/j.jsb.2016.07.005](https://doi.org/10.1016/j.jsb.2016.07.005).
- [30] I.Silva Barreto, S. Le Cann, S. Ahmed, V. Sotiriou, M.J. Turunen, U. Johansson, A. Rodriguez-Fernandez, T.A. Grünwald, M. Liebi, N.C. Nowlan, H. Isaksson, Multiscale characterization of embryonic long bone mineralization in mice, *Adv. Sci.* 7 (2020) 1–13, doi:[10.1002/advs.202002524](https://doi.org/10.1002/advs.202002524).
- [31] R.K. Fuchs, M.R. Allen, K.W. Condon, S. Reinwald, L.M. Miller, D. McClenathan, B. Keck, R.J. Phipps, D.B. Burr, Strontium ranelate does not stimulate bone formation in ovariectomized rats, *Osteoporos. Int.* 19 (2008) 1331–1341, doi:[10.1007/s00198-008-0602-6](https://doi.org/10.1007/s00198-008-0602-6).
- [32] T. Fischer, R. Riedl, Molecular recognition of the catalytic zinc(II) ion in MMP-13: structure-based evolution of an allosteric inhibitor to dual binding mode inhibitors with improved lipophilic ligand efficiencies, *Int. J. Mol. Sci.* (2016) 17, doi:[10.3390/ijms17030314](https://doi.org/10.3390/ijms17030314).
- [33] M. Tägil, M.M. McDonald, A. Morse, L. Peacock, K. Mikulec, N. Amanat, C. Godfrey, D.G. Little, Intermittent PTH(1–34) does not increase union rates in open rat femoral fractures and exhibits attenuated anabolic effects compared to closed fractures, *Bone* 46 (2010) 852–859, doi:[10.1016/j.bone.2009.11.009](https://doi.org/10.1016/j.bone.2009.11.009).
- [34] P. Bosemark, H. Isaksson, M.M. McDonald, D.G. Little, M. Tägil, Augmentation of autologous bone graft by a combination of bone morphogenic protein and bisphosphonate increased both callus volume and strength, *Acta Orthop.* 84 (2013) 106–111, doi:[10.3109/17453674.2013.773123](https://doi.org/10.3109/17453674.2013.773123).
- [35] O. Bunk, M. Bech, T.H. Jensen, R. Feidenhans'l, T. Binderup, A. Menzel, F. Pfeiffer, Multimodal x-ray scatter imaging, *New J. Phys.* (2009) 11, doi:[10.1088/1367-2630/11/12/123016](https://doi.org/10.1088/1367-2630/11/12/123016).
- [36] C.N. Borca, D. Grolimund, M. Willmann, B. Meyer, K. Jefimovs, J. Vila-Comamala, C. David, The microXAS beamline at the swiss light source: Towards nano-scale imaging, *J. Phys. Conf. Ser.* 186 (2009) 8–11, doi:[10.1088/1742-6596/186/1/012003](https://doi.org/10.1088/1742-6596/186/1/012003).
- [37] V.A. Solé, E. Papillon, M. Cotte, P. Walter, J. Susini, A multiplatform code for the analysis of energy-dispersive X-ray fluorescence spectra, *Spectrochim. Acta Part B: At. Spectrosc.* 62 (2007) 63–68, doi:[10.1016/j.sab.2006.12.002](https://doi.org/10.1016/j.sab.2006.12.002).
- [38] G. Ashtiotis, A. Deschildre, Z. Nawaz, J.P. Wright, The fast azimuthal integration Python library, *pyFAI res. pap.* (2015) 510–519, doi:[10.1107/S1600576715004306](https://doi.org/10.1107/S1600576715004306).
- [39] L.C. Bonar, A.H. Roufosse, W.K. Sabine, M.D. Grynaps, M.J. Glimcher, X-ray diffraction studies of the crystallinity of bone mineral in newly synthesized and density fractionated bone, *Calcif. Tissue Int.* 35 (1983) 202–209, doi:[10.1007/BF02405032](https://doi.org/10.1007/BF02405032).
- [40] U. Johansson, D. Carbone, S. Kalbfleisch, A. Björling, M. Kahnt, S. Sala, T. Stankevics, M. Liebi, A.R. Fernandez, B. Bring, D. Paterson, K. Thanell, P. Bell, D. Erb, C. Weninger, R. Matej, L. Roslund, K. Ahnberg, B.N. Jensen, H. Tarawneh, A. Mikkelsen, U. Vogt, NanoMAX: the hard X-ray nanoprobe beamline at the MAX IV laboratory, *J. Synchrotron Radiat.* 28 (2021) 1935–1947, doi:[10.1107/S1600577521008213](https://doi.org/10.1107/S1600577521008213).
- [41] D. Carbone, S. Kalbfleisch, U. Johansson, A. Björling, M. Kahnt, S. Sala, T. Stankevics, A. Rodriguez-Fernandez, B. Bring, Z. Matej, P. Bell, D. Erb, V. Hardion, C. Weninger, H. Al-Sallami, J. Lidon-Simon, S. Carlson, A. Jerrebo, B.N. Jensen, A. Bjermo, K. Ahnberg, L. Roslund, Design and performance of a dedicated coherent X-ray scanning diffraction instrument at beamline NanoMAX of MAX IV, *J. Synchrotron Radiat.* 29 (2022) 876–887, doi:[10.1107/S1600577522001333](https://doi.org/10.1107/S1600577522001333).
- [42] N. Mathavan, M.J. Turunen, M. Guizar-Sicairos, M. Bech, F. Schaff, M. Tägil, H. Isaksson, The compositional and nano-structural basis of fracture healing in healthy and osteoporotic bone, *Sci. Rep.* 8 (2018) 1–12, doi:[10.1038/s41598-018-19296-z](https://doi.org/10.1038/s41598-018-19296-z).
- [43] N. Mathavan, D.B. Raina, M. Tägil, H. Isaksson, Longitudinal in vivo monitoring of callus remodeling in BMP-7- and Zoledronate-treated fractures, *J. Orthop. Res.* 38 (2020) 1905–1913, doi:[10.1002/jor.24632](https://doi.org/10.1002/jor.24632).
- [44] S. Haumont, Distribution of Zn in bone tissue, *J. Histochem. Cytochem.* 005 (1960), doi:[10.1177/9.2.141](https://doi.org/10.1177/9.2.141).
- [45] D.A. Bradley, C.J. Moger, C.P. Winlove, Zn deposition at the bone-cartilage interface in equine articular cartilage, *Nucl. Instruments Methods Phys. Res. Sect. A* 580 (2007) 473–476, doi:[10.1016/j.nima.2007.05.143](https://doi.org/10.1016/j.nima.2007.05.143).
- [46] W. Kaabar, O. Gundogdu, A. Lakloul, O. Bunk, F. Pfeiffer, M.J. Farquharson, D.A. Bradley, μ -PIXE and SAXS studies at the bone-cartilage interface, *Appl. Radiat. Isot.* 68 (2010) 730–734, doi:[10.1016/j.apradiso.2009.09.038](https://doi.org/10.1016/j.apradiso.2009.09.038).
- [47] A. Roschger, J.G. Hofstaetter, B. Pemmer, N. Zoeger, P. Wobraschek, G. Falkenberg, R. Simon, A. Berzlanovich, H.W. Thaler, P. Roschger, K. Klaushofer, C. Strelj, Differential accumulation of lead and zinc in double-tidemarks of articular cartilage, *Osteoarthritis Cartil.* 21 (2013) 1707–1715, doi:[10.1016/j.joca.2013.06.029](https://doi.org/10.1016/j.joca.2013.06.029).
- [48] M. Rauwolf, B. Pemmer, A. Roschger, A. Turyanskaya, S. Smolek, A. Maderitsch, P. Hischenhuber, M. Foelser, R. Simon, S. Lang, S.E. Puchner, R. Windhager, K. Klaushofer, P. Wobraschek, J.G. Hofstaetter, P. Roschger, C. Strelj, Increased

- zinc accumulation in mineralized osteosarcoma tissue measured by confocal synchrotron radiation micro X-ray fluorescence analysis, *X-Ray Spectrom.* 46 (2017) 56–62, doi:[10.1002/xrs.2727](https://doi.org/10.1002/xrs.2727).
- [49] B.R. Genge, G.R. Sauer, L.N.Y. Wu, F.M. McLean, R.E. Wuthier, Correlation between loss of alkaline phosphatase activity and accumulation of calcium during matrix vesicle-mediated mineralization, *J. Biol. Chem.* 263 (1988) 18513–18519, doi:[10.1016/s0021-9258\(19\)81388-1](https://doi.org/10.1016/s0021-9258(19)81388-1).
- [50] T.M. Litchfield, Y. Ishikawa, L.N.Y. Wu, R.E. Wuthier, G.R. Sauer, Effect of metal ions on calcifying growth plate cartilage chondrocytes, *Calcif. Tissue Int.* 62 (1998) 341–349, doi:[10.1007/s002239900442](https://doi.org/10.1007/s002239900442).
- [51] M. Nagata, B. Lönnerdal, Role of zinc in cellular zinc trafficking and mineralization in a murine osteoblast-like cell line, *J. Nutr. Biochem.* 22 (2011) 172–178, doi:[10.1016/j.jnutbio.2010.01.003](https://doi.org/10.1016/j.jnutbio.2010.01.003).
- [52] D. Zhu, Y. Su, M.L. Young, J. Ma, Y. Zheng, L. Tang, Biological Responses and Mechanisms of Human Bone Marrow Mesenchymal Stem Cells to Zn and Mg Biomaterials, *ACS Appl. Mater. Interfaces.* 9 (2017) 27453–27461, doi:[10.1021/acsami.7b06654](https://doi.org/10.1021/acsami.7b06654).
- [53] H.C. Anderson, Matrix vesicles and calcification, *Curr. Rheumatol. Rep.* 5 (2003) 222–226, doi:[10.1007/s11926-003-0071-z](https://doi.org/10.1007/s11926-003-0071-z).
- [54] M. Yamaguchi, M.N. Weitzmann, Zinc stimulates osteoblastogenesis and suppresses osteoclastogenesis by antagonizing NF- κ B activation, *Mol. Cell. Biochem.* 355 (2011) 179–186, doi:[10.1007/s11010-011-0852-z](https://doi.org/10.1007/s11010-011-0852-z).
- [55] D.M. Medeiros, Copper, iron, and selenium dietary deficiencies negatively impact skeletal integrity: a review, *Exp. Biol. Med.* 241 (2016) 1316–1322, doi:[10.1177/1535370216648805](https://doi.org/10.1177/1535370216648805).
- [56] J. Díaz-Castro, M.R. López-Frías, M.S. Campos, M. López-Frías, M.J.M. Alférez, T. Nestares, M.L. Ojeda, I. López-Aliaga, Severe nutritional iron-deficiency anaemia has a negative effect on some bone turnover biomarkers in rats, *Eur. J. Nutr.* 51 (2012) 241–247, doi:[10.1007/s00394-011-0212-5](https://doi.org/10.1007/s00394-011-0212-5).
- [57] M. Parelman, B. Stoecker, A. Baker, D. Medeiros, Iron restriction negatively affects bone in female rats and mineralization of hFOB osteoblast cells, *Exp. Biol. Med.* 231 (2006) 378–386, doi:[10.1177/153537020623100403](https://doi.org/10.1177/153537020623100403).
- [58] D.M. Medeiros, A. Plattner, D. Jennings, B. Stoecker, Bone morphology, strength and density are compromised in iron-deficient rats and exacerbated by calcium restriction, *J. Nutr.* 132 (2002) 3135–3141, doi:[10.1093/jn/131.10.3135](https://doi.org/10.1093/jn/131.10.3135).
- [59] D.M. Medeiros, B. Stoecker, A. Plattner, D. Jennings, M. Haub, Iron deficiency negatively affects vertebrae and femurs of rats independently of energy intake and body weight, *J. Nutr.* 134 (2004) 3061–3067, doi:[10.1093/jn/134.11.3061](https://doi.org/10.1093/jn/134.11.3061).
- [60] I. Bertini, V. Calderone, M. Fragai, C. Luchinat, M. Maletta, J.Y. Kwon, Snapshots of the reaction mechanism of matrix metalloproteinases, *Angew. Chemie - Int. Ed.* 45 (2006) 7952–7955, doi:[10.1002/anie.200603100](https://doi.org/10.1002/anie.200603100).
- [61] M.J. Hackett, J.A. McQuillan, F. El-Assaad, J.B. Aitken, A. Levina, D.D. Cohen, R. Siegle, E.A. Carter, G.E. Grau, N.H. Hunt, P.A. Lay, Chemical alterations to murine brain tissue induced by formalin fixation: Implications for biospectroscopic imaging and mapping studies of disease pathogenesis, *Analyst* 136 (2011) 2941–2952, doi:[10.1039/c0an00269k](https://doi.org/10.1039/c0an00269k).
- [62] H. Malluche, M. Faugere, 7 Technique of Mineralized Bone Histology (1986), doi:[10.1159/000412204](https://doi.org/10.1159/000412204).